

<sup>1</sup> 3D/2D Projected Shape Sensitivity Analysis of Total Joint Arthroplasty  
<sup>2</sup> Implants

<sup>3</sup> Andrew James Jensen<sup>a</sup>, Kerry E. Costello<sup>a</sup>, Catia S. Silva<sup>b</sup>, Scott A. Banks<sup>a</sup>

<sup>a</sup>*Department of Mechanical and Aerospace Engineering, University of Florida, Gainesville, Florida, U.S.A.*

<sup>b</sup>*Department of Electrical and Computer Engineering, University of Florida, Gainesville, Florida, U.S.A.*

---

<sup>4</sup> **Abstract**

Recent advancements in computer vision and machine learning have facilitated fully autonomous kinematics measurement of Total Knee Arthroplasty (TKA) implant components from single-plane fluoroscopic images. However, such performance has yet to be effectively replicated for Reverse Total Shoulder Arthroplasty (rTSA) implants. This study examines the correlation between 3D implant orientation and the shape sensitivity of their 2D projections, employing the Invariant Angular Radial Transform Descriptor (IARTD). It was observed that minor rotational differences along near-symmetric dimensions, such as the humeral internal/external rotation and the tibial internal/external axis, resulted in negligible shape alterations. Moreover, axes that posed challenges in registration were associated with reduced sensitivity of the shape descriptor. The findings indicate that symmetrical geometries and orientations inherently limit the amount of pose information that can be extracted from a single-projection silhouette. Nevertheless, the inclusion of bony anatomical landmarks as optimization constraints emerges as a promising approach to mitigate ambiguity and enhance registration accuracy.

<sup>5</sup> **Keywords:** Computer vision, TKA, rTSA, Shape Descriptor, Angular Radial Transform

---

<sup>6</sup> **1. Introduction**

<sup>7</sup> Understanding the in-vivo kinematics of total joint replacement has been essential in implant design,  
<sup>8</sup> post-operative assessment, and predicting wear and failure patterns for nearly three decades [1–3]. Recent  
<sup>9</sup> advancements in computer vision and machine learning have enabled these analyses for total knee arthro-  
<sup>10</sup> plasty (TKA) in a fully autonomous and clinically practical setting, utilizing single-plane fluoroscopy [4, 5].  
<sup>11</sup> However, using only a single camera inherently limits the measurement accuracy due to loss of depth percep-  
<sup>12</sup> tion and the introduction of ambiguous projected shapes during optimization [6–9]. The observed limitation,

Table 1: Root mean squared differences between JointTrack Machine Learning optimized kinematics and manually registered kinematics on single-plane fluoroscopy

Implant Type	$x_{trans}(mm)$	$y_{trans}(mm)$	$z_{trans}(mm)$	$x_{rot}(\circ)$	$y_{rot}(\circ)$	$z_{rot}(\circ)$
Humeral	8.46	8.64	152.78	22.59	64.74	11.81
Glenosphere	0.97	1.44	32.58	13.72	26.40	8.30
Femoral	0.57	0.39	26.95	0.66	0.73	0.60
Tibial	0.67	0.64	27.17	1.63	2.74	0.66

13 predominantly impacting mediolaterally symmetric tibial implants, led to a phenomenon termed “symmetry  
 14 traps.” In such instances, two distinct three-dimensional orientations of the implant produce indistinguish-  
 15 able two-dimensional projected geometries. A machine learning algorithm was developed to address these  
 16 symmetry traps in symmetric tibial implants. This algorithm was trained to recognize accurate anatomic  
 17 orientations and correct images caught in optimization minima [10]. However, this approach required the  
 18 symmetric implant to register into one of the two potential local minima, each corresponding to a distinct  
 19 “symmetry trap.”

20 The application of the same optimization routine and cost function [5, 6] to reverse total shoulder arthro-  
 21 plasty (rTSA) resulted in significantly lower performance compared to its application in TKA implants  
 22 (Table 1) [5]. This suboptimal performance manifested primarily along the internal/external rotation axis,  
 23 which has salient features often occluded by the glenosphere implant in frontal-plane fluoroscopy (Fig. 1).  
 24 Additionally, this axis is nearly rotationally symmetric for both the humeral and glenospere implants. Poor  
 25 rotation registration also increases translation errors, as the silhouette shape of the estimated pose is wholly  
 26 different from the fluoroscopic image, causing imprecise translation alignment along all axes. In a manual  
 27 registration setting [11], different combinations of model and image views are utilized to overcome these  
 28 limitations (Fig. 2).

29 The current investigation delves into the fundamental shape aspects of each arthroplasty system, with a  
 30 focus on developing a method for autonomously measuring rTSA kinematics from single-plane fluoroscopy.  
 31 Central to this is the use of Invariant Shape Descriptors, particularly the Invariant Angular Radial Transform  
 32 Descriptor (IARTD), which offers a mathematically robust approach to describe object shapes [12]. These  
 33 descriptors are immune to variations in scale, translation, or orientation [13], and are adept at quantifying the  
 34 relative “nearness”, “farness”, and “uniqueness” of shapes as vector differences. Such properties are valuable



Figure 1: A representative example of poor internal/external rotation of the humeral implant after automated model-image registration using JointTrack Machine Learning [5].

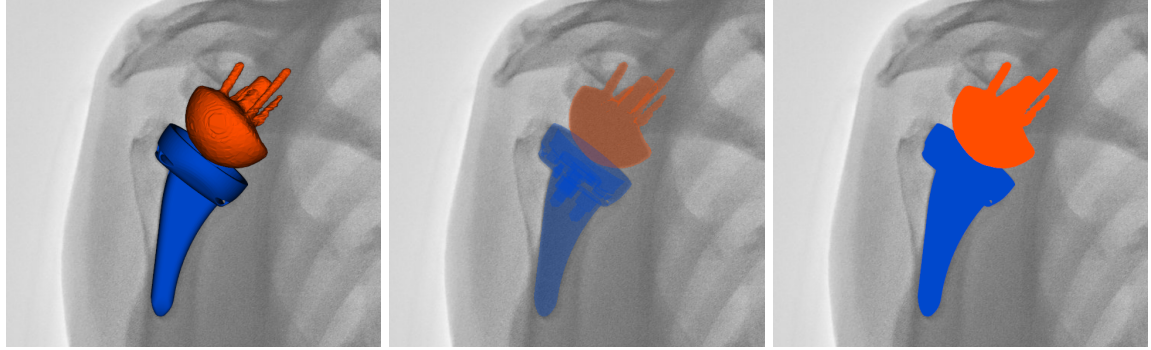


Figure 2: Some different model views of a manually registered humeral and glenoid implant in an rTSA system. Of note, each view gives the user a different type of feature to focus on. The original view allows the user to determine the relative orientation based on shading, the transparent view allows the user to see the underlying fluoroscopic image, and the solid view allows the user to focus on specific regions of error. Each is crucial to performing manual registration.

<sup>35</sup> for object categorization [14–16] and kinematics measurement [9], with IARTD’s sensitivity to radial shape  
<sup>36</sup> differences [12] being particularly beneficial for detailed contour analysis.

<sup>37</sup> The focus of this analysis is on the sensitivity of projected 2D shapes, as depicted by IARTD, to changes  
<sup>38</sup> in their 3D orientation. This is key to understanding the impact of subtle orientation variations on the  
<sup>39</sup> projected shape, an aspect integral to shape-based optimization metrics. The ultimate aim is to highlight  
<sup>40</sup> performance differences in autonomous kinematics measurements between TKA and rTSA implant systems.  
<sup>41</sup> Additionally, the study seeks to identify areas where imaging methods can be improved to boost the algo-  
<sup>42</sup> rithm’s performance.

43 **2. Methods**

44 *2.1. Data Collection*

45 For shape sensitivity analysis, representative 3D models of rTSA humeral and glenosphere implants, as  
46 well as TKA femoral and tibial implants, were obtained from a manufacturer. The study focused on a single  
47 size for each implant type, as the scale of the shapes was normalized using an Invariant Shape Descriptor,  
48 rendering multiple sizes unnecessary for this analysis.

49 *2.2. Image Generation*

50 Each implant's binary silhouette was rendered to a  $1024 \times 1024$  image plane using an in-house CUDA  
51 camera model (CUDA Version 12.1) [17]. The model featured a 1000mm focal length and 0.3mm per pixel  
52 resolution, which are quite typical projection parameters for fluoroscopic images. All imaging tasks utilized  
53 an NVIDIA Quadro P2200 GPU.

54 *2.3. Invariant Angular Radial Transform*

55 The Invariant Angular Radial Transform Descriptor (IARTD) was selected for its radial direction sen-  
56 sitivity, enabling the detection of subtle contour changes in projected shapes [12]. This sensitivity allows  
57 us to address minor changes along the contour of the projected shape, which is a desirable property for  
58 determining the minor changes in shape with respect to input orientation.

59 IARTD computation involves aggregating orthogonal basis components across the unit polar disk, forming  
60 a complex moment. Each basis function has an order ( $n$ ) and a repetition ( $p$ ). The order can be visualized  
61 as concentric rings on the polar disk, and the repetition as the count of slices partitioning the unit disk along  
62  $\theta$ . For these calculations, the image is normalized so that the center is at  $(0, 0)$ , and the four corners are at  
63  $(\pm 1, \pm 1)$ .

64 Each angular radial transform (ART) coefficient is a complex double integral (Eq. 1) over the image in  
65 polar coordinates,  $f(\rho, \theta)$  multiplied by the ART basis function,  $V_{np}(\rho, \theta)$  (Eq. 2).

$$F_{np} = \int_0^{2\pi} \int_0^1 f(\rho, \theta) V_{np}(\rho, \theta) \rho d\rho d\theta \quad (1)$$

$$V_{np}(\rho, \theta) = A_p(\theta)R_n(\rho) \quad (2)$$

66 The radial basis function includes a complex exponential,  $A_p(\theta)$  (Eq. 3), ensuring rotational invariance,  
 67 and a trigonometric transform,  $R_p(\theta)$  (Eq. 4), to establish orthogonality.

$$A_p(\theta) = \frac{1}{2\pi} e^{jp\theta} \quad (3)$$

68

$$R_n(\rho) = \begin{cases} 1 & n = 0 \\ 2 \cos(\pi n \rho) & n \neq 0 \end{cases} \quad (4)$$

69 Phase correction is applied to each ART coefficient (Eq. 5, Eq. 6) to adjust for differences in in-plane  
 70 rotation.

$$\phi'_{np} = \phi_{np} - \phi_{n,1} \quad (5)$$

$$F'_{np} = F_{np} e^{-jp\phi_{n,1}} \quad (6)$$

71 Subsequently, the final feature vector is formulated by the polar decomposition of each coefficient at  
 72 every order and repetition (Eq. 7). Values from the first two repetitions are excluded, as they do not provide  
 73 significant information [12]. The complete IARTD feature vector encompasses values of  $n = 0, \dots, 3$  and  
 74  $p = 0, \dots, 8$  per the original authors' suggestion [12].

$$IARTD = \{|F'_{np}|, \phi'_{np}\} \text{ where } n \geq 0, p \geq 2 \quad (7)$$

75 *2.4. Shape Differences and Sensitivity*

76 In order to quantify the overall change between shapes, a readily interpretable value must be established.  
 77 To simplify notation, successive rotations are denoted as subscripts, with  $R_z R_x R_y$  being represented as  
 78  $R_{z,x,y}$ . If more than 3 rotations are applied successively, the full rotation sequence will be captured as

79  $R_{r_1, r_2, r_3, \dots, r_n}$ . Similarly, the application of the IARTD equation to an implant at a specific input orientation  
 80  $R_{z,x,y}$  is denoted as  $IARTD(R_{z,x,y})$ . Shape differences were calculated using the central difference equation  
 81 on the IARTD vector produced from two different orientations. The grid of sampled orientations had extrema  
 82 of  $\pm 30^\circ$  with a step size of  $5^\circ$  for each of the  $x$ ,  $y$ , and  $z$  axes. The “differences” along each axis were computed  
 83 using a positive and negative rotation ( $\pm\delta$ ) of 1 degree . Therefore, for every set of  $x, y, z$  rotations, three  
 84 distinct shape differences are computed, one each for  $\delta_x$ ,  $\delta_y$ , and  $\delta_z$  (Eq. 8).

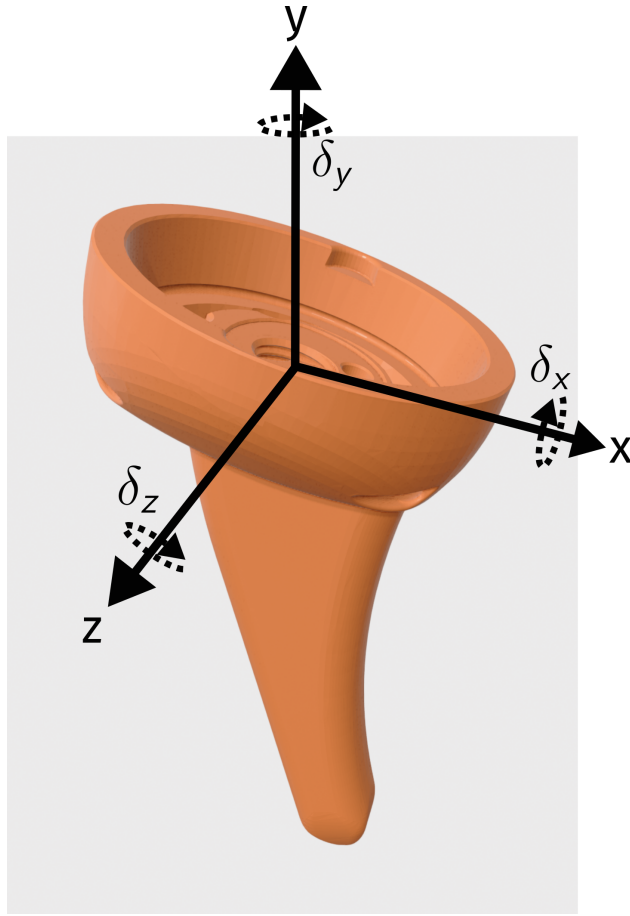


Figure 3: A generic manufacturer-provided humeral implant with label x, y, and z rotation axis. Additionally, each of the  $\delta_x, \delta_y$ , and  $\delta_z$  are shown, corresponding to the rotational directions of each shape descriptor difference.

85 For notational brevity, we will condense the total equation to a single  $\Delta S(\delta)$ , (representing  $\Delta Shape$  for  
 86 a differential rotation  $\delta$ ).

$$\begin{aligned} \Delta S(\delta)_{z,x,y} &\equiv IARTD(R_{z,x,y,+\delta}) \\ &\quad - IARTD(R_{z,x,y,-\delta}) \end{aligned} \tag{8}$$

$\forall \delta \in \{\delta_x, \delta_y, \delta_z\}$

87        The disparate scales of IARTD vector elements necessitate their normalization, ensuring a balanced  
 88        assessment of global behavior without overemphasis on any individual element. Z-scaling provides a practical  
 89        approach to normalizing each element relative to its distribution. After z-scaling, the Euclidean norm of  
 90        each  $S(\delta)_{z,x,y}$  is calculated to quantify the total shape change for a specific differential rotation (Eq. 9).

91        The final step takes advantage of two factors: first, that the in-plane rotations are the first in the Euler  
 92        sequence ( $z$ -axis), and second, that this type of rotation does not affect the in-plane shape. For each  $x$   
 93        and  $y$  input rotation, an average is computed from values where  $x$  and  $y$  remain constant while  $z$  varies  
 94        (Eq. 10). The final values are obtained from this equation, denoted by  $\mathbb{S}$ . Individual plots were created for  
 95         $\mathbb{S}_{x,y}$ , corresponding to each differential rotation in  $x$ ,  $y$ , and  $z$ , and for each of the four implant types. An  
 96        analysis of these plots were conducted to assess the performance of JTML optimization and to explore areas  
 97        where low shape-sensitivity will pose significant challenges for registration-based optimization.

$$\|S(\delta)_{z,x,y}\|_2 \tag{9}$$

$$\mathbb{S}(\delta)_{x,y} = \frac{\sum_z \|S(\delta)_{z,x,y}\|_2}{N} \tag{10}$$

### 98        3. Results

99        The humeral implant exhibited the lowest mean  $\mathbb{S}(\delta_y)$  across all implant types (Fig. 4) (Table 2). This ro-  
 100      tation represents the final rotation in our Euler rotation sequence (Z-X-Y) and captures the internal/external  
 101      rotation of the humeral implant. Additionally, the surface plotted by the humeral shape sensitivity for all  
 102       $\delta_{x,y,z}$  is much smoother than any of the other plots, demonstrating the relative lack of shape difference for  
 103      a wide range of input orientations. Several plots showed regions with relatively low sensitivity. Specifically,

Table 2: Average projected-shape sensitivity values for each of the implant models.

Implant Type	Average $\bar{S}(\delta_x)$	Average $\bar{S}(\delta_y)$	Average $\bar{S}(\delta_z)$
Humeral	8.83	4.82	7.08
Glenosphere	6.37	6.22	4.86
Femoral	6.88	8.68	4.93
Tibial	9.0	5.52	3.72

104 the glenosphere's  $\delta_y$  sensitivity along the  $y = 0$  axis (Fig. 5) and the tibial implant's  $\delta_y$  sensitivity along the  
 105  $x = 0$  axis (Fig. 7). The femoral implant had the highest average sensitivity ( $\frac{\bar{S}(\delta_x) + \bar{S}(\delta_y) + \bar{S}(\delta_z)}{3}$ ) among all  
 106 implant types .

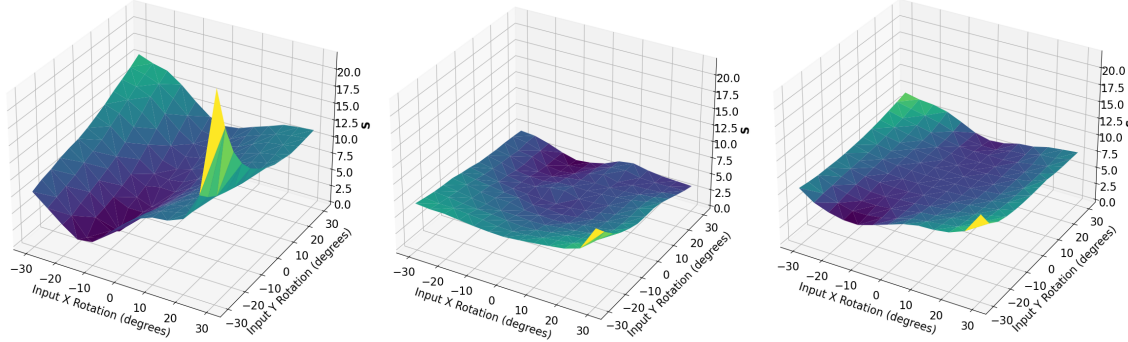


Figure 4: The  $\bar{S}$  plot for a humeral implant for  $\delta$  rotations along the x, y, and z axis, respectively.

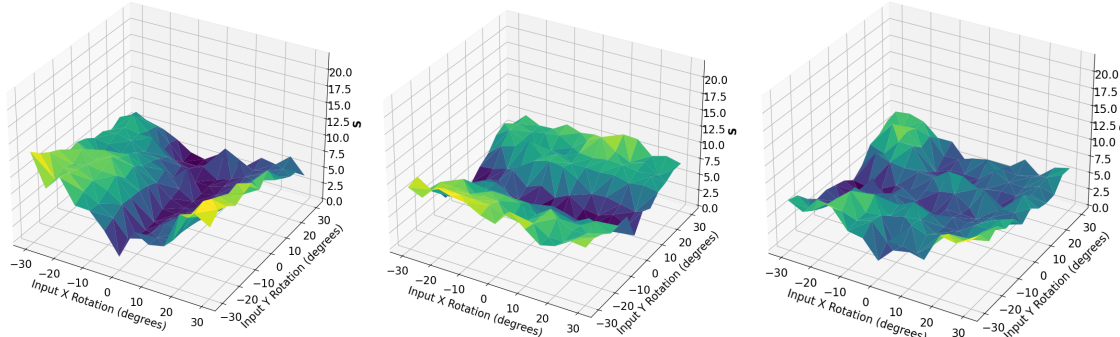


Figure 5: The  $\bar{S}$  plot for a glenosphere implant for  $\delta$  rotations along the x, y, and z axis, respectively.

#### 107 4. Discussion

108 The findings correspond closely with initial expectations regarding the sensitivity measurement of pro-  
 109 jected shapes relative to 3D object orientation and are consistent with areas challenging for JTML optimiza-  
 110 tion. Specifically, the humeral implant showed a generally smooth and minimal shape sensitivity profile,  
 111 particularly for  $\delta_y$  rotations (Table 2). Along this axis, the humeral implant is the most cylindrical, meaning

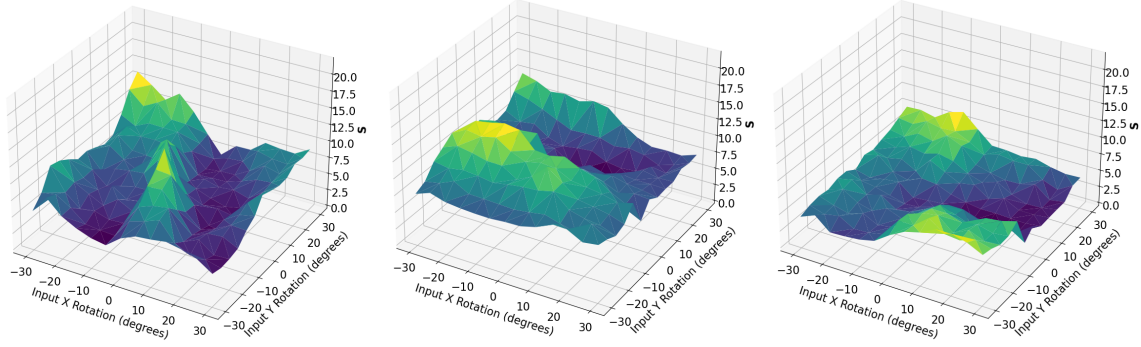


Figure 6: The  $\mathbb{S}$  plot for a femoral implant for  $\delta$  rotations along the x, y, and z axis, respectively.

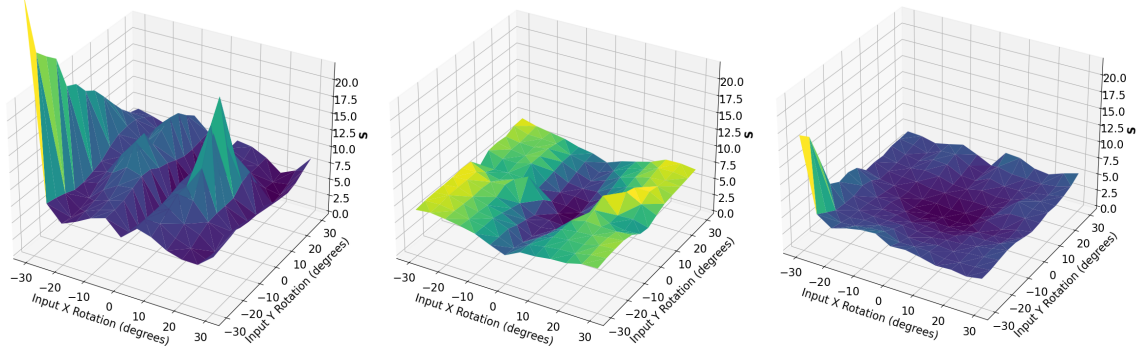


Figure 7: The  $\mathbb{S}$  plot for a tibial implant for  $\delta$  rotations along the x, y, and z axis, respectively.

112 we would not expect to see a significant change in the shape descriptor with minor  $\delta_y$  rotations. Furthermore,  
 113 it is noteworthy that this axis presented the most significant difficulties in JTML optimization.

114 Similar intuitive outcomes are observed with the glenosphere implant, which exhibited the lowest average  
 115  $\mathbb{S}(\delta)$  among all the implant types. This implant primarily consists of an articulation surface closely approx-  
 116 imating a spherical shape. Given that the projection of a sphere (a circle) remains constant regardless of  
 117 the sphere's orientation, the closer a shape is to a spherical form, the lower its overall shape sensitivity is  
 118 expected to be.

119 The observed shape sensitivity of the tibial implant with respect to  $\delta_y$  rotation aligns with the concept  
 120 of symmetry traps. There is a consistently low shape sensitivity along the line where  $x = 0$ . This axis,  
 121 associated with internal/external rotation, is the same one that contributes to symmetry traps, where two  
 122 different 3D orientations result in an identical projected shape. In terms of this analysis, the  $\Delta S$  value would  
 123 be 0 for these two orientations of the tibial implant.

124 This study sheds light on an important aspect of JointTrack Machine Learning, particularly the use of

125 Euler angles in the DIRECT-JTA optimization routine. Currently, the optimization does not involve in-  
126 dependently varying all angles within a body-centered reference frame, as this approach is not conducive  
127 to hyperbox creation [6, 18]. Instead, optimization is performed over a range of ordered rotations, pro-  
128 jected through the sequence  $R_z R_x R_y$ . The challenges the humeral implant encounters in aligning the  $y$ -axis  
129 illustrate that this ordered sequence, especially with a symmetric final axis, can hinder the convergence  
130 process.

131 Beyond the inherent shape sensitivities, such optimization limitations motivate exploring alternatives to  
132 Euler angles. Performing registration optimization directly on the Special Orthogonal group  $SO(3)$  poses an  
133 intriguing direction.  $SO(3)$  encapsulates all possible 3D rotations in a mathematically convenient structure  
134 (A *Lie Group*, which is both a manifold and a group) [19, 20]. By optimizing on this manifold instead of  
135 Euler angle parametrizations, issues with gimbal lock and cascading rotation effects can be avoided. However,  
136 most manifold optimization is specifically tailored to derivative-based optimization, which is not currently  
137 supported by the DIRECT-JTA algorithm that JointTrack Machine Learning incorporates [5, 6, 18]. This  
138 limitation motivates either a restructuring of the current optimization methods to incorporate derivative  
139 information, or to explore the potentials of derivative-free (black-box) optimization [21] over manifolds.

140 Historical manual registration software heavily relied on bony landmarks within images to disambiguate  
141 challenging implant poses. As landmarks, the tibial tuberosity, fibula, and bicipital groove were vital in iden-  
142 tifying the specific orientation of implants, all of which are visible and utilized by the user in a manual regis-  
143 tration setting (Fig. 2). To accurately assess implant kinematics in highly symmetric unicompartmental knee  
144 arthroplasty, surface meshes of femoral and tibial components were incorporated into the registration pro-  
145 cess [22]. These bone models were particularly beneficial in addressing implants’ internal/external rotation  
146 along semi-symmetric axes. Additionally, the use of densely selected keypoints in the precise measurement  
147 of preoperative shoulder kinematics through biplane fluoroscopy has been documented [23], with keypoint  
148 registration achieved via a modified Perspective-N-Points optimization routine. Furthermore, intensity-  
149 based metrics have played a crucial role in the accurate determination of healthy tibiofemoral kinematics  
150 [24]. Rather than minimizing the Euclidean distance of projected model keypoints, these methods leverage  
151 digitally reconstructed radiographs and directly compare the intensity values of the x-ray image and the

152 projection estimate. Thus, utilizing bony landmarks for measuring implant kinematics presents a robust and  
153 reliable approach to measuring accurate joint kinematics in clinical environments.

154 **5. Conclusion**

155 This study demonstrates intrinsic differences between implant types regarding projected 2D shape sen-  
156 sitivity. Measurement difficulties aligned with low sensitivity along problematic axes—humeral internal  
157 rotation and tibial symmetry traps. Fundamentally, small orientation changes yielded negligible 2D vari-  
158 ability for near-symmetrical geometries and axes. While inherent shape constraints limit data extractable  
159 solely from single-plane fluoroscopic silhouettes, incorporating additional image information like bone offers  
160 promise. Despite unavoidable ambiguity along select dimensions, boosting descriptor sensitivity and em-  
161 ploying precise anatomical constraints could enable robust clinical tracking. Overall, relating optimization  
162 performance to shape response underscores routes toward accurate autonomous kinematic analysis.

163 **References**

- 164 [1] B. J. Fregly, W. Sawyer, M. K. Harman, S. A. Banks, Computational wear prediction of a to-  
165 tal knee replacement from in vivo kinematics, *Journal of Biomechanics* 38 (2) (2005) 305–314.  
166 doi:10.1016/j.jbiomech.2004.02.013.
- 167 [2] S. A. Banks, W. Hodge, 2003 Hap Paul Award paper of the International Society for Technology in  
168 Arthroplasty, *The Journal of Arthroplasty* 19 (7) (2004) 809–816. doi:10.1016/j.arth.2004.04.011.
- 169 [3] S. A. Banks, E. Deckard, W. A. Hodge, R. M. Meneghini, Rationale and Results for Fixed-Bearing  
170 Pivoting Designs in Total Knee Arthroplasty, *The Journal of Knee Surgery* 32 (07) (2019) 590–595.  
171 doi:10.1055/s-0039-1679924.
- 172 [4] J. S. Broberg, J. Chen, A. Jensen, S. A. Banks, M. G. Teeter, Validation of a machine learning technique  
173 for segmentation and pose estimation in single plane fluoroscopy, *Journal of Orthopaedic Research* (Feb.  
174 2023). doi:10.1002/jor.25518.

- 175 [5] A. J. Jensen, P. D. Flood, L. S. Palm-Vlasak, W. S. Burton, A. Chevalier, P. J. Rullkoetter, S. A.  
176 Banks, Joint Track Machine Learning: An Autonomous Method of Measuring Total Knee Arthroplasty  
177 Kinematics From Single-Plane X-Ray Images, *The Journal of Arthroplasty* 38 (10) (2023) 2068–2074.  
178 doi:10.1016/j.arth.2023.05.029.
- 179 [6] P. D. L. Flood, S. A. Banks, Automated registration of 3-D knee implant models to fluoroscopic im-  
180 ages using lipschitzian optimization, *IEEE Transactions on Medical Imaging* 37 (1) (2018) 326–335.  
181 doi:10.1109/tmi.2017.2773398.
- 182 [7] M. Mahfouz, W. Hoff, R. Komistek, D. Dennis, A robust method for registration of three-dimensional  
183 knee implant models to two-dimensional fluoroscopy images, *IEEE Transactions on Medical Imaging*  
184 22 (12) (2003) 1561–1574. doi:10.1109/TMI.2003.820027.
- 185 [8] S. Zuffi, A. Leardini, F. Catani, S. Fantozzi, A. Cappello, A model-based method for the reconstruction  
186 of total knee replacement kinematics, *IEEE Transactions on Medical Imaging* 18 (10) (Oct./1999) 981–  
187 991. doi:10.1109/42.811310.
- 188 [9] S. Banks, W. Hodge, Accurate measurement of three-dimensional knee replacement kinematics us-  
189 ing single-plane fluoroscopy, *IEEE Transactions on Biomedical Engineering* 43 (6) (1996) 638–649.  
190 doi:10.1109/10.495283.
- 191 [10] A. J. Jensen, C. S. Silva, K. E. Costello, S. A. Banks, Correcting Symmetric Implant Ambiguity in  
192 Measuring Total Knee Arthroplasty Kinematics from Single-Plane Fluoroscopy (In Review).
- 193 [11] S. Mu, JointTrack: An Open-Source, Easily Expandable Program for Skeletal Kinematic Measurement  
194 Using Model-Image Registration (2007) 27.
- 195 [12] J.-M. Lee, W.-Y. Kim, A New Shape Description Method Using Angular Radial Transform, *IEICE*  
196 *Transactions on Information and Systems* E95.D (6) (2012) 1628–1635. doi:10.1587/transinf.E95.D.1628.
- 197 [13] D. Zhang, G. Lu, Review of shape representation and description techniques, *Pattern Recognition* 37 (1)  
198 (2004) 1–19. doi:10.1016/j.patcog.2003.07.008.

- 199 [14] C. W. Richard, H. Hemami, Identification of Three-Dimensional Objects Using Fourier Descriptors of  
200 the Boundary Curve, *IEEE Transactions on Systems, Man, and Cybernetics SMC-4* (4) (1974) 371–378.  
201 doi:10.1109/TSMC.1974.5408458.
- 202 [15] T. P. Wallace, O. R. Mitchell, Analysis of three-dimensional movement using Fourier descrip-  
203 tors, *IEEE Transactions on Pattern Analysis and Machine Intelligence PAMI-2* (6) (1980) 583–588.  
204 doi:10.1109/TPAMI.1980.6447707.
- 205 [16] T. P. Wallace, P. A. Wintz, An efficient three-dimensional aircraft recognition algorithm using  
206 normalized fourier descriptors, *Computer Graphics and Image Processing* 13 (2) (1980) 99–126.  
207 doi:10.1016/S0146-664X(80)80035-9.
- 208 [17] J. Nickolls, I. Buck, M. Garland, K. Skadron, Scalable Parallel Programming with CUDA, *ACM Queue*  
209 6 (2) (2008) 40–53.
- 210 [18] D. R. Jones, C. D. Perttunen, B. E. Stuckman, Lipschitzian optimization without the Lipschitz constant,  
211 *Journal of Optimization Theory and Applications* 79 (1) (1993) 157–181. doi:10.1007/BF00941892.
- 212 [19] W. Ziller, Lie Groups. Representation Theory and Symmetric Spaces, University of Pennsylvania (2010).
- 213 [20] J.-P. Serre, Lie Algebras and Lie Groups: 1964 Lectures given at Harvard University, 2nd Edition, no.  
214 1500 in *Lecture Notes in Mathematics*, Springer-Verlag, Berlin ; New York, 1992.
- 215 [21] C. Audet, W. Hare, Derivative-Free and Blackbox Optimization, Springer Series in Operations Research  
216 and Financial Engineering, Springer International Publishing, Cham, 2017. doi:10.1007/978-3-319-  
217 68913-5.
- 218 [22] S. A. Banks, B. J. Fregly, F. Boniforti, C. Reinschmidt, S. Romagnoli, Comparing in vivo kinematics of  
219 unicondylar and bi-unicondylar knee replacements, *Knee Surgery, Sports Traumatology, Arthroscopy*  
220 13 (7) (2005) 551–556. doi:10.1007/s00167-004-0565-x.
- 221 [23] W. Burton, I. R. Crespo, T. Andreassen, M. Pryhoda, A. Jensen, C. Myers, K. Shelburne, S. Banks,  
222 P. Rullkoetter, Fully automatic tracking of native glenohumeral kinematics from stereo-radiography,  
223 *Computers in Biology and Medicine* 163 (2023) 107189. doi:10.1016/j.combiomed.2023.107189.

- <sup>224</sup> [24] N. Baka, M. de Bruijne, T. van Walsum, B. L. Kaptein, J. E. Giphart, M. Schaap, W. J. Niessen,  
<sup>225</sup> B. P. F. Lelieveldt, Statistical Shape Model-Based Femur Kinematics From Biplane Fluoroscopy, IEEE  
<sup>226</sup> Transactions on Medical Imaging 31 (8) (2012) 11.